COMMUNICATION

Crystal Flexibility Design through Local and Global Motility Cooperation

Ping Wang, [a] Ken-ichi Otake,* [a] Nobuhiko Hosono, [a,b] and Susumu Kitagawa*[a]

[a] Dr. P. Wang, Prof. Dr. K. Otake, Prof. Dr. N. Hosono Prof. Dr. S. Kitagawa
Institute for Integrated Cell-Material Sciences (WPI-iCeMS),
Kyoto University Institute for Advanced Study, Kyoto University
Yoshida Ushinomiya-cho, Sakyo-ku, Kyoto 606-8501 (Japan)
E-mail: ootake.kenichi.8a@kyoto-u.ac.jp
kitagawa@icems.kyoto-u.ac.jp

[b] Prof. Dr. N. Hosono
Department of Advanced Materials Science,
Graduate School of Frontier Sciences, The University of Tokyo,
5-1-5 Kashiwanoha, Kashiwa, Chiba 277-8561, (Japan)

Supporting information for this article is given via a link at the end of the document.

Abstract: Incorporating local mobility into a flexible framework promises to create cooperative properties unattainable in a conventional soft porous crystal. In this study, we propose a design strategy that integrates substituent moieties and a flexible porous crystal framework via intra-framework π-π interactions. This integration not only facilitates framework structural transitions but also gives the porous coordination polymers (PCPs) different guest-free structures that depend on the activation conditions. The incorporated flexibility gives the material the ability to discriminate C6 alkane isomers based on different gate-opening behaviors. Thus, the PCP has potential applications in C6 isomer separation, a critical step in the petroleum refining process to produce gasoline with high octane rating. This strategy, based on ligand designability, offers a new approach to flexible PCP structural and functional design.

Flexible porous coordination polymers (PCP) are characterized by reversible structural transitions that originate from a global lattice change triggered by guest uptake and release.[1-7] This reversible structural transformation, which is termed gate-opening behavior, occurs at a certain threshold pressure (a gate-opening pressure).[8-18] This feature can endow flexible PCPs with an exclusive molecular discrimination capability, which thus makes them of interest as separation media.[19-25] However, a rational control strategy of flexible PCP remains elusive. Recently, local motion of the dynamic entities in rigid PCP pores has also drawn interest. These moieties can form rigid PCPs with an adaptive nature and selectivity by regulating the guest diffusion inside the pore.[26-29]

Incorporation of local dynamics into flexible frameworks is a promising method for creating cooperative flexibility that is unattainable in conventional PCPs.[30] Efforts to this end have been attempted by introducing dynamic sidearms into the pillar of flexible PCPs;[31-33] however, novel cooperative properties, other than an altered gate-opening pressure, have not been demonstrated. This lack of progress might be attributed to a lack of interactions that integrate motion of the substituents and framework and regulate the behavior of structural transitions.

Herein, we proposed a rational incorporation strategy that connects a flexible framework and mobile fragments through intra-framework π-π interactions (Figure 1). The stacking arenes adjust position synergistically during a structural transition, endowing this PCP substituent-framework cooperative flexibility. The synchronized motion confines the ligands' spatial position, preventing the framework pores from collapsing upon solvent removal, and facilitates the framework structural transition at a relatively small gate-opening pressure. Furthermore, the flexibility integration recasts the system energy landscape, enabling the PCP to adopt various guest-free structures depending on the activation conditions, either thermal or supercritical drying. In contrast, isostructural PCPs without π-π interactions deform without restraint into a compact closed structure with gate-opening behavior that is triggered with difficulty by guest molecules regardless of the activation approach.

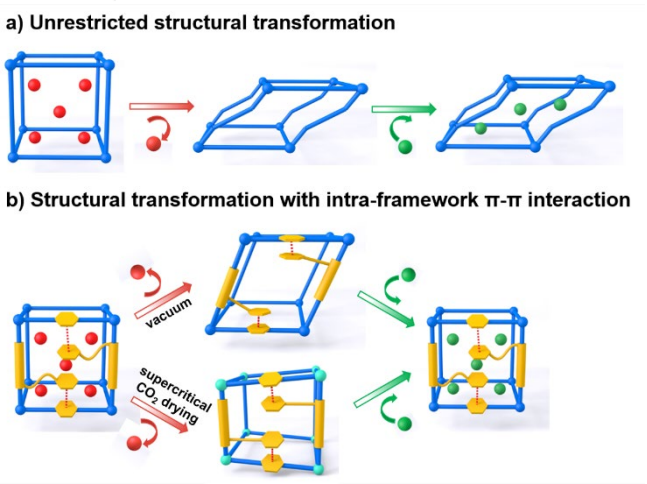

(a) Conventional flexible PCPs undergo unrestricted deformation after solvent removal, transforming to a specific close phase; if the framework deforms severely, the compact close phase can not be reopened by guest molecules. (b) PCP with local and global flexibility integrated by π-π interaction. The interaction restricts the PCP deformation, leading to various porous guest-free structures that can be reopened by guest molecule inclusion.

To introduce the dynamic aromatic substituents, we first designed functionalized 1,4-benzenedicarboxylic acid (H_2bdc) ligands, decorated with mobile aromatic substituents. The aromatic substituents were connected by short alkane chains, which facilitated stacking of the substituent's stacking with neighbor ligands. It has previously been theoretically[34] and

experimentally[35-36] shown that electron-withdrawing groups relieve the electrostatic repulsion between arenes and facilitate π-π stacking. For this reason, we synthesized two ligands for comparison: 2,5-bis[(2-nitrobenzyl)oxy]-1,4-benzenedicarboxylic acid (H_2bdc-NO_2) with an electron-withdrawing nitro group and 2,5-bis(benzyloxy)-1,4-benzenedicarboxylic acid (H_2bdc-H) with a benzyl substituent (Figure 2a).

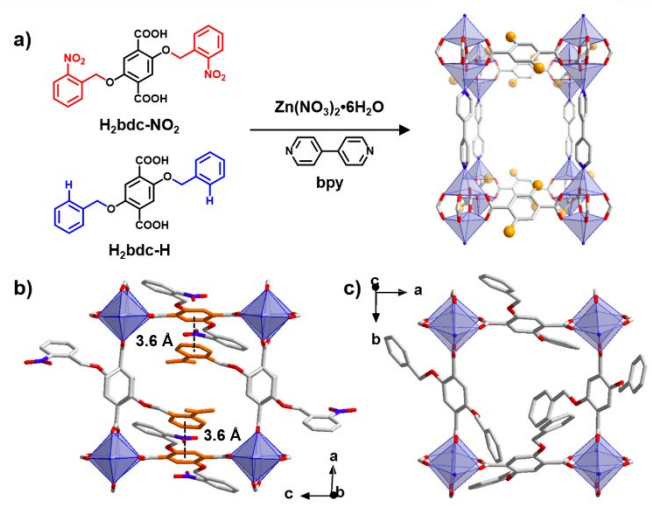

Figure 2. a) 3D pillared-layer PCPs synthesized by aromatic substituents bearing ligand, $Zn(NO_3)_2·6H_2O$, and bipyridine. Top view of as-synthesized b) **1-NO_2** and c) **1-H**. Aromatic parts involved in the π-π interaction are highlighted in orange. Atoms are colored as follows: Zn, purple; C, gray; N, blue; O, red. Hydrogen atoms and solvent molecules are omitted for clarity. The dashed line and numbers mark the center distance of arenes that form π-π dimers.

Single crystals were obtained by a solvothermal reaction in the presence of $Zn(NO_3)_2·6H_2O$, 4,4'-bipyridine (bpy), and the aromatic substituent bearing a 1,4-benzenedicarboxylic acid. Single crystal X-ray diffraction (SXRD) analyses revealed that the two PCPs were isostructural and characterized by a non-interpenetrated 3D pillared-layer structure with the chemical formula of $[Zn_2(bdc\text{-}R)_2(bpy)]·(solvent)_n\}$ (**1-R**) (Figures 2; R = NO_2 or H). bdc-R ligands and Zn_2 paddlewheel clusters formed 2D square grid-like layers, further connected by bpy pillar ligands to form 3D frameworks.

According to SXRD analysis, parallel π-π stacking occurred for **1-NO_2**. The nitro-substituted arenes stack with the central benzene of bdc-NO_2 ligand, forming a π-π interactive dimer with a center distance of 3.6 Å and a dihedral angle of 8.6° (Figure 2b). The aromatic substituents aligned in channels along the *b* axis with the nitro groups pointing toward the channel center, dividing the PCP channels into isolated cages with a void space of 10.8% (Figure S1). Conversely, in **1-H**, all the appended benzenes anchored at the corner of the channel and remained perpendicular to the nearest bdc-H ligand (dihedral angle = 86.6°) (Figure S2). This vertical conformation eliminated the possibility of π-π interactions between benzyl substituents and bdc-H by minimizing stacking. Thus, the **1-H** 3D channels had a void space as high as 34.3%. We observed CH…π interactions between benzyl substituents with a dihedral angle of central benzene and CH…π distance of 88.5° and 2.9 Å, respectively.

Solvent molecules accommodated in the as-synthesized PCPs were exchanged with acetonitrile before 80 °C thermal activation in a vacuum, which was confirmed by thermogravimetric analyses (TGA; Figures S3–S4). After activation, the guest-free **1-NO_2** (**1-NO_2-vac**) had a sharp powder X-ray diffraction (PXRD) pattern distinct from that of the as-synthesized one, as confirmed by the disappearance of the peak at 6.28° (Figure 3a). Conversely, the thermally activated **1-H** (**1-H-vac**) had a broad PXRD signal with a single intense peak at 6.52° (Figure 3b). The structural transformation of both PCPs was reversible, as indicated by the recovery of the PXRD patterns after soaking in *N,N*-Dimethylformamide (DMF) at room temperature.

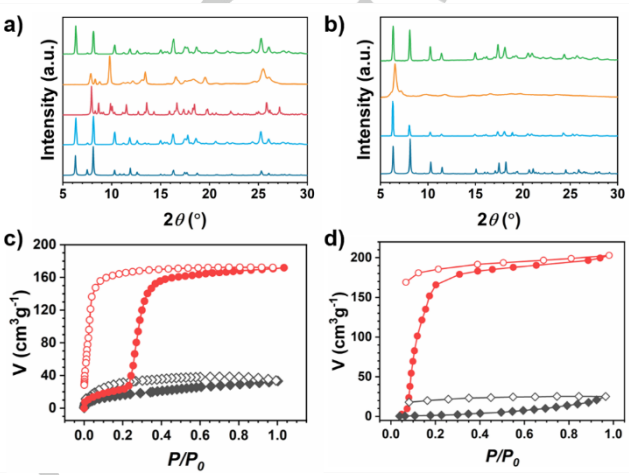

Figure 3. a) Powder X-ray diffraction patterns (PXRD) of **1-NO_2** simulated from as-synthesized single crystal (indigo), **1-NO_2** experimental (blue), **1-NO_2-vac** simulated from thermal activated single crystal (red), **1-NO_2-vac** experimental (orange), and **1-NO_2-vac** regenerated from DMF (green). b) PXRD of **1-H** simulated from as-synthesized single crystal (indigo), **1-H** experimental (blue), **1-H-vac** experimental (orange), and **1-H-vac** regenerated from DMF (green). Adsorption isotherms of **1-NO_2-vac** (red circles) and **1-H-vac** (black squares) for c) CO_2 at 195 K and d) toluene at 298 K. Closed symbols denote adsorption and empty symbols denote desorption.

The N_2 (77 K) and CO_2 (195 K) adsorption isotherms were measured to test the PCP flexibility and porosity. Though both adsorbed trace amounts of N_2 because of its small pore size (Figures S5–S6), distinct uptake behavior of **1-NO_2-vac** and **1-H-vac** was observed in CO_2 sorption. **1-NO_2-vac** had a typical gate-opening type adsorption isotherm for CO_2: an initial uptake of 28 mL g^{-1} before the gate-opening pressure at P/P_0 = 0.23 and a saturated capacity of 172 mL g^{-1} after the structural transformation (Figure 3c). The desorption isotherm does not trace the adsorption curve and sharply decreased at P/P_0 = 0.1. The sharp adsorption increase and desorption decrease with the hysteresis indicate that the structural transformation was triggered by CO_2 adsorption, as further supported by changes of the in-situ PXRD patterns under various CO_2 pressures (Figure S7). Conversely, **1-H-vac** did not have gate-opening behavior for CO_2 at atmospheric pressure, resulting in a small capacity of 33 mL g^{-1} (Figures 3c, S8). Adsorption behaviors of other gas and vapor species were also measured. **1-NO_2-vac** had gate-open type adsorption for C_2H_4 (170 K, P/P_0 = 0.06) (Figure S9), C_2H_6 (185 K, P/P_0 = 0.20) (Figure S10), and toluene (298 K, P/P_0 = 0.08) (Figure 3d). Conversely, **1-H-vac** had only a small uptake of these guests without a gate-open transformation (Figure 3c–d, Figures S9–10).

To uncover the reason for the distinctive sorption behaviors of the isostructural PCPs, we used variable-temperature powder X-ray diffraction (VTPXRD) to monitor the guest solvent removal process. The PXRD pattern of as-synthesized **1-H** was maintained up to 80 °C but transformed gradually from 80 °C to 120 °C. At 120 °C, the structural transformation was completed, and the resulting pattern had only one broad peak at 6.52°, which is assigned to the PCP inter-layer distance (Figure S11). Diffraction signals from 2D grid layers all faded and disappeared during thermal activation, as exemplified by the (200) peak relating to the distance between bdc-H ligands (Figure S12). The changes of the VTPXRD indicate that upon DMF removal, **1-H** lost its long-range order in the *a* and *c* directions, and the ordered grids of the $[Zn(bdc\text{-}H)]_n$ 2D layer collapsed.

Unlike the gradual transition of **1-H**, the VTPXRD of **1-NO₂** underwent an abrupt structural change at 90 °C (Figure S13). To elucidate the reason for the rapid change of **1-NO₂**, we examined single crystals of **1-NO₂-vac** by SXRD. Diffraction analyses of **1-NO₂-vac** confirmed that the framework connectivity was the same as that of **1-NO₂**; however, the space group changed from monoclinic *P2/c* to triclinic *P–1* (Table S1). **1-NO₂-vac** underwent slippage between layers and the interlayer distance decreased from 14.0 Å (**1-NO₂**) to 10.8 Å (**1-NO₂-vac**) (Figure 4a). Notably, despite the considerable interlayer shrinkage, the π-π stacking dimers were well preserved in the grid of $[Zn(bdc\text{-}NO_2)]_n$ layers (Figure 4b). In **1-NO₂-vac**, 50% of the dimers were almost identical to those of the as-synthesized **1-NO₂** with the same focal distance (3.6 Å) (Figure 4b, orange part); the other 50% rearranged, such that the bdc-NO_2 ligand and nitrobenzyl substituent rotated along the *c* axis, yielding a stacking distance of 3.7 Å (Figure 4b, green part). Because the two-types of π-π dimers were distributed in two neighboring grids separately, the 2D layer was corrugated.

The VTPXRD results confirmed that in the absence of intra-framework π-π interactions (**1-H**), the long-range order of the 2D grid layers was easily disrupted upon guest removal; whereas in the case of intra-framework π-π interactions (**1-NO₂**), the crystal-to-crystal structural transition occurred when π-π stacking dimers were maintained even after thermal activation. Therefore, we attribute the differences between the isostructural PCPs to the substituent-framework π-π interaction. These interactions confined the ligands spatial position and maintained the π-π stacking configuration, thus restraining distortion of the 2D-grid. Consequently, the π-π interaction-controlled deformation created a porous guest-free framework that could be reopened by guest molecules. Conversely, unrestrained deformation yielded compact-close **1-H-vac** disordered 2D layers that required an unpractically high gate-opening pressure (Figure 2c, d, and Figures S9-S10). Our assumption was further tested by investigating isostructural PCP with the bdc-Me ligand (**1-Me**, Figures S14–S17). The as-synthesized **1-Me** had weak π-π interactions with a 3.8 Å stacking distance, which is longer than that those of **1-NO₂** (3.6 Å). As expected from the stabilization effect of π-π stacking dimers, for CO_2 and toluene adsorption, guest-free **1-Me-vac** had gate-opening behavior but a large gate-opening pressure compared with **1-NO₂-vac** (Figures S18–S19).

When we activated **1-NO₂** by supercritical CO_2, we obtained an activated phase (**1-NO₂-SCO₂**) unlike that of the thermally activated one (**1-NO₂-vac**) (Figures S20–S21). The SXRD structure determination of **1-NO₂-SCO₂** shows that the framework connectivity changed because zinc ions varied in their coordination environment (Figure 4c). In **1-NO₂-SCO₂**, one carboxylate out of four became monodentate and the Zn_2 paddlewheel deformed. The cluster deformation compressed the space between the 2D layers, resulting in two kinds of 1D channels along the *c* axis. In the cluster distorted grids, π-π stacking between the nitrobenzyl substituents and the bdc-NO_2 ligand was retained (Figure 4d). The stacking distance of the 50% π-π interaction increased from 3.6 to 3.7 Å because of Zn-O bond cleavage. Unlike **1-NO₂-vac**, two stacking types coexisted in every grid of **1-NO₂-SCO₂**. **1-NO₂-SCO₂** was readily opened by CO_2 at 195 K, as characterized by a gate-opening pressure of P/P_0 = 0.37 (Figure S22). Conversely, the supercritical CO_2 activated **1-H** (**1-H-SCO₂**) had a broad PXRD pattern and flat CO_2 uptake similar to that of **1-H-vac** (Figures S23–S25). The SXRD results confirm that **1-NO₂-SCO₂** maintained its structure even at 80 °C when activated for 12 h and did not transform to **1-NO₂-vac**.

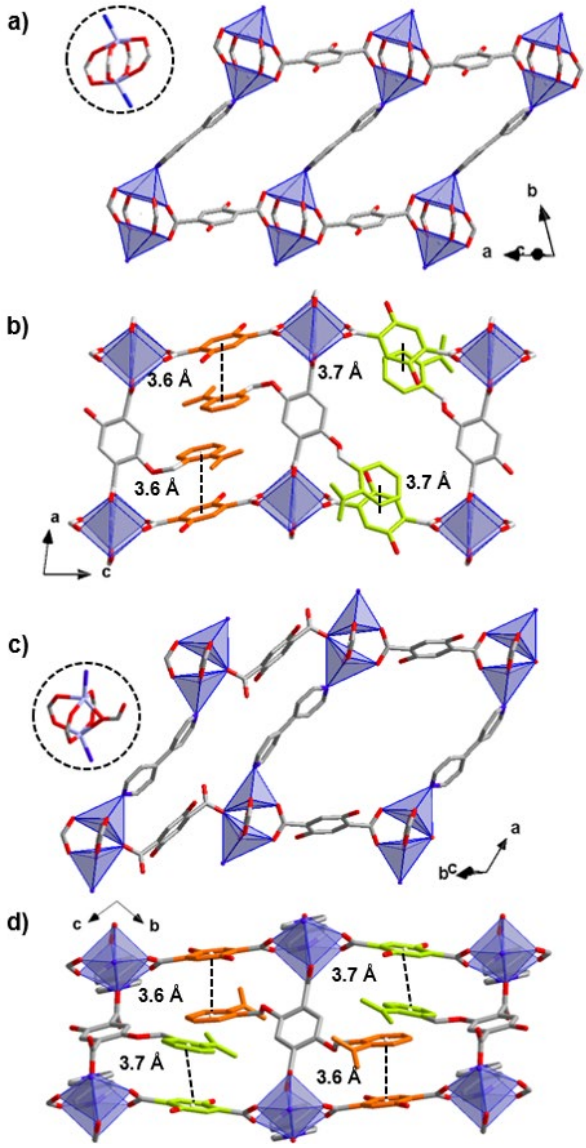

Figure 4. Structure of guest-free **1-NO₂**. a) Side and b) top view of vacuum activated **1-NO₂-vac**. c) Side and d) top view of supercritical CO_2 activated **1-NO₂-SCO₂**. The coordination environment of the Zn_2 paddlewheel clusters is shown in the inset. Aromatic parts involved in the π-π interactions are highlighted in orange and green. Atoms are colored as follows: Zn, purple; C,

gray; N, blue; O, red. Hydrogen atoms are omitted. The dashed line and numbers mark the center distance of arenes that formed π-π dimers.

To uncover the reason for the **1-NO$_2$** structural dependence on the activation approach, crystal structures of guest-free PCPs were compared. Despite the differently deformed frameworks of **1-NO$_2$-vac** and **1-NO$_2$-SCO$_2$**, their π-π stacking configurations were similar. In the absence of intra-framework π-π interactions (**1-H**), the 2D grid layers, composed of bdc and Zn_2 paddlewheel clusters, deformed during the activation (Figures S11-12). In **1-NO$_2$**, the π-π attraction locked the layer distortion, recasting the soft system energy landscape. To stabilize the guest-free frameworks, different deformation routes were followed: the interlayer slippage in **1-NO$_2$-vac** and the cluster switch in **1-NO$_2$-SCO$_2$**. After thermal activation, the angles between the bpy pillar and the 2D grid layer changed from 90° in **1-NO$_2$** to 46° in **1-NO$_2$-vac,** and the Zn_2 clusters from neighbor layers linked by each bpy shifted to 7.6 Å. While after supercritical drying, the bpy pillars in **1-NO$_2$-SCO$_2$** tilted with respect to the 2D grid layer only at an angle of 67° in accompany with the shift of the Zn_2 cluster to 6.5 Å. The most striking change in **1-NO$_2$-SCO$_2$** is that the Zn_2 paddlewheel cluster changes its structure: one out of eight Zn-O bonds cleaved. The conditions such as solvents, temperature, and pressure play a crucial role in flexible PCP structural changes. Unlike thermal activation in vacuo, supercritical CO_2 activation applied high pressure to liquefy CO_2, which could cause the structural change of Zn_2 cluster in **1-NO$_2$**. Subsequently, in-pore CO_2 solvents were removed without surface tension, resulting in **1-NO$_2$-SCO$_2$**. Thus, we assumed the deformation difference of PCP **1-NO$_2$** might result from structural stress induced by varied activation approaches.[37]

C6 alkane isomers are the main components of gasoline, including linear *n*-hexane (HEX), mono-branched 3-methylpentane (3MP), and di-branched 2,2-dimethylbutane (2,2DMB). C6 sorting is a vital process in industrial gasoline upgrading because only 2,2DMB is desirable for refined gasoline because of its high research octane number (RON).[38] Several PCPs have been investigated for C6 isomer sorting; however, all suffer from the poor selectivity.[39-41] We posit that the aromatic substituents that crowd the 1D channels are able to form CH-π interactions with C6 molecules. The soft nature of the PCPs can discriminate against differences in the host-guest interactions, leading to varied gate-opening behavior. To test this hypothesis, we performed C6 isomer vapor adsorption measurements.

Single-component vapor adsorption at 30 °C indicated the perfect discrimination performance of **1-NO$_2$-vac**: HEX was adsorbed by the gate-opening process (P_{go}/P_{sat} = 0.09) with a saturated capacity of 145 mg g^{-1}; 3MP induced no gate-opening adsorption but instead had a linear isotherm with 41 mg g^{-1} capacity; 2,2DMB was completely size-excluded with no adsorption (Figure 5 and Figures S26–S27). On the contrary, **1-NO$_2$-SCO$_2$** had gate-opening adsorption to HEX, but was unable to uptake either 3MP or 2,2DMB (Figure S28); **1-H-vac** prevented entrance of all isomers into its pore (Figures S29–S30). Therefore, the low porosity of **1-NO$_2$-SCO$_2$** and the large gate-opening pressure of **1-H-vac** rendered these materials unsuitable for isomer discrimination.

In summary, we have developed a crystal flexibility design strategy by integrating substituent and framework motility via intra-framework π-π interactions of ligands. The flexible and synchronous movement confined framework distortion upon solvent removal, giving PCPs with different porous guest-free structures that depend on the activation approach. These PCPs discriminated between C6 alkane isomers by a distinct gate-opening behavior. These features suggest potential for applications as an isomer splitter for gasoline upgrading. The availability of various aromatic substituents and designability of PCPs enables the creation of an aromatic π-π interactions between local mobility and soft porous crystals. This structure in turn provides a new chemical approach for flexible PCP structural and functional design.

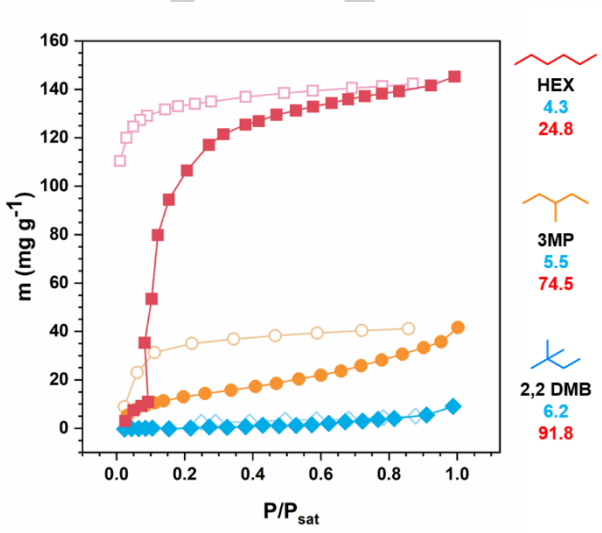

Figure 5. 1-NO$_2$-vac adsorption isotherms at 303 K for HEX (red), 3MP (yellow), and 22DMB (blue). Closed symbols denote adsorption, and empty symbols denote desorption. Kinetic diameter (blue number, in Å) and RON (red number) of each isomer is marked below the chemical structure.

Acknowledgements

This study was supported by KAKENHI Grants-in-Aid for Scientific Research (S) (JP18H05262), and Early-Career Scientists (JP19K15584), and Scientific Research (B) (JP18H02072) and Scientific Research on Innovative Areas “Molecular Engine” (JP19H05381) from the Japan Society for the Promotion of Science (JSPS). NMR spectroscopy was performed at the iCeMS Analysis Center, Kyoto University Institute for Advanced Study. We thank Nanae Shimanaka at iCeMS, Kyoto University, for her contributions to SXRD analysis.

Keywords: porous coordination polymer • flexibility • motility cooperation • activation method • molecular recognition

[1] S. Kitagawa, R. Kitaura, S. Noro, *Angew. Chem. Int. Ed.* **2004**, *43*, 2334-2375.
[2] S. Horike, S. Shimomura, S. Kitagawa, *Nat. Chem.* **2009**, *1*, 695-704.
[3] A. Schneemann, V. Bon, I. Schwedler, I. Senkovska, S. Kaskel, R. A. Fischer, *Chem. Soc. Rev.* **2014**, *43*, 6062-6096.
[4] Z. Chang, D.-H. Yang, J. Xu, T.-L. Hu, X.-H Bu, *Adv. Mater.* **2015**, *27*, 5432-5441.
[5] T. D.Bennett, A. K.Cheetham, A. H.Fuchs, F.-X. Coudert, *Nat. Chem.* **2017**, *9*, 11-16.

[6] S. K. Elsaidi, M. H. Mohamed, D. Banerjee, P. K. Thallapally, *Coord. Chem. Rev.* **2018,** *358*, 125-152.
[7] F. Bigdeli, C. T. Lollar, A. Morsali, H. C. Zhou, *Angew. Chem. Int. Ed.* **2020,** *59*, 4652-4669.
[8] B.-Q. Song, Q.-Y. Yang, S.-Q. Wang, M. Vandichel, A. Kumar, C. Crowley, N. Kumar, C.-H. Deng, V. GasconPerez, M. Lusi, H. Wu, W. Zhou, M. J. Zaworotko, *J. Am. Chem. Soc.* **2020,** *142*, 6896-6901.
[9] P. H. Dominik, A. K. Ryan, A. B. Michael, A. T. Benjamin, M. B. Craig, R. L. Jeffrey, *Chem. Sci.* **2020**, *11*, 6709-6716.
[10] T. Kundu, M. Wahiduzzaman, B. B. Shah, G. Maurin, D. Zhao, *Angew. Chem. Int. Ed.* **2019,** *58*, 8073-8077.
[11] S. Suginome, H. Sato, A. Hori, A. Mishima, Y. Harada, S. Kusaka, R. Matsuda, J. Pirillo, Y. Hijikata, T. Aida, *J. Am. Chem. Soc.* **2019,** *141*, 15649-15655.
[12] S. Kusaka, A. Kiyose, H. Sato, Y. Hijikata, A. Hori, Y. Ma, R. Matsuda, *J. Am. Chem. Soc.* **2019,** *141*, 15742-15746.
[13] A. X. Zhu, Q. Y. Yang, S. Mukherjee, A. Kumar, C. H. Deng, A. A. Bezrukov, M. Shivanna, M. J. Zaworotko, *Angew. Chem. Int. Ed.* **2019,** *58*, 18212-18217.
[14] M.-H. Yu, B. Space, D. Franz, W. Zhou, C. He, L. Li, R. Krishna, Z. Chang, W. Li, T.-L. Hu, X.-H. Bu, *J. Am. Chem. Soc.* **2019**, *141*, 17703-17712.
[15] M. Souto, J. Romero, J. Calbo, I. J. Vitórica-Yrezábal, J. L. Zafra, J. Casado, E. Ortí, A. Walsh, G. Mínguez Espallargas, *J. Am. Chem. Soc.* **2018**, *140*, 10562-10569.
[16] Y. Hui, G. Feng, L. Prem, G. Wen-Yang, W. Hui, J. B. Leonard, Z. Wei, Z. Jian, A. Briana, M. Shengqian, *ACS Cent. Sci.* **2018,** *4*, 1194-1200.
[17] Y. T. Zheng, H. Sato, P. Y. Wu, H. J. Jeon, R. Matsuda, S. Kitagawa, *Nat. Commun.* **2017,** *8*, 100.
[18] Q. Gao, J. Xu, D. Cao, Z. Chang, X.-H. Bu, *Angew. Chem. Int. Ed.* **2016**, *55*, 15027-15030.
[19] Y. Yan, E. J. Carrington, R. Pétuya, G. F. S. Whitehead, A. Verma, R. K. Hylton, C. C. Tang, N. G. Berry, G. R. Darling, M. S. Dyer, D. Antypov, A. P. Katsoulidis, M. J. Rosseinsky, *J. Am. Chem. Soc.* **2020,** *142*, 14903-14913.
[20] Y. Gu, J.-J. Zheng, K.-i. Otake, K. Sugimoto, N. Hosono, S. Sakaki, F. Li, S. Kitagawa, *Angew. Chem. Int. Ed.* **2020**, *59*, 15517 –15521.
[21] H. Sato, W. Kosaka, R. Matsuda, A. Hori, Y. Hijikata, R. V. Belosludov, S. Sakaki, M. Takata, S. Kitagawa, *Science* **2014,** *343*, 167.
[22] D.-D. Zhou, P. Chen, C. Wang, S.-S. Wang, Y. Du, H. Yan, Z.-M. Ye, C.-T. He, R.-K. Huang, Z.-W. Mo, N.-Y. Huang, J.-P. Zhang, *Nat. Mater.* **2019,** *18*, 994-998.
[23] S. Sen, N. Hosono, J. J. Zheng, S. Kusaka, R. Matsuda, S. Sakaki, S. Kitagawa, *J. Am. Chem. Soc.* **2017,** *139*, 18313-18321.
[24] L. Li, R.-B. Lin, R. Krishna, X. Wang, B. Li, H. Wu, J. Li, W. Zhou, B. Chen, *J. Am. Chem. Soc.* **2017,** *139*, 7733-7736.
[25] M. L. Foo, R. Matsuda, Y. Hijikata, R. Krishna, H. Sato, S. Horike, A. Hori, J. Duan, Y. Sato, Y. Kubota, M. Takata, S. Kitagawa, *J. Am. Chem. Soc.* **2016,** *138*, 3022-3030.
[26] S. Horike, R. Matsuda, D. Tanaka, S. Matsubara, M. Mizuno, K. Endo, S. Kitagawa, *Angew. Chem. Int. Ed.* **2006,** *45*, 7226-7230.
[27] D. I. Kolokolov, H. Jobic, A. G. Stepanov, V. Guillerm, T. Devic, C. Serre, G. Férey, *Angew. Chem. Int. Ed.* **2010,** *49*, 4791-4794.
[28] K. Zhu, C. A. O'Keefe, V. N. Vukotic, R. W. Schurko, S. J. Loeb, *Nat. Chem.* **2015,** *7*, 514-519.
[29] C. Gu, N. Hosono, J.-J. Zheng;, Y. Sato, S. Kusaka, S. Sakaki, S. Kitagawa, *Science* **2019,** *363*, 387.
[30] S. Krause, N. Hosono, S. Kitagawa, *Angew. Chem. Int. Ed.* **2020,** *59,* 15325-15341.
[31] J. Seo, R. Matsuda, H. Sakamoto, C. Bonneau, S. Kitagawa, *J. Am. Chem. Soc.* **2009,** *131*, 12792-12800.
[32] S. Henke, A. Schneemann, A. Wutscher, R. A.Fischer, *J. Am. Chem. Soc.* **2012,** *134*, 9464-9474.
[33] S. Jeoung, S. Lee, J. H. Lee, S. Lee, W. Choe, D. Moon, H. R. Moon, *Chem. Commun.* **2019,** *55*, 8832-8835.
[34] M. O. Sinnokrot, C. D. Sherrill, *J. Am. Chem. Soc.* **2004,** *126*, 7690-7697.
[35] F. Cozzi, M. Cinquini, R. Annuziata, J. S. Siegel, *J. Am. Chem. Soc.* **1993,** *115*, 5330-5331.
[36] F. Cozzi, M. Cinquini, R. Annunziata, T. Dwyer, J. S. Siegel, *J. Am. Chem. Soc.* **1992,** *114*, 5729-5733. Wang, H.; Li, J. *Acc. Chem. Res.* **2019,** *52*, 1968-1978.
[37] A. P. Nelson, O. K. Farha, K. L. Mulfort, J. T. Hupp, *J. Am. Chem. Soc.* **2009,** *131*, 458-460
[38] H. Wang, J. Li, *Acc. Chem. Res.* **2019,** *52*, 1968-1978.
[39] P. S. Bárcia, F. Zapata, J. A. C. Silva, A. E. Rodrigues, B. Chen, *J. Phys. Chem. B* **2007,** *111*, 6101-6103.
[40] Z. R. Herm, B. M. Wiers, J. A. Mason, J. M. van Baten, M. R. Hudson, P. Zajdel, C. M. Brown, N. Masciocchi, R. Krishna, J. R. Long, *Science* **2013,** *340*, 960.
[41] H. Wang, X. Dong, J. Lin, S. J. Teat, S. Jensen, J. Cure, E. V. Alexandrov, Q. Xia, K. Tan, Q. Wang, D. H. Olson, D. M. Proserpio, Y. J. Chabal, T. Thonhauser, J. Sun, Y. Han, J. Li, *Nat. Commun.* **2018,** *9*, 1745.

Entry for the Table of Contents

Insert graphic for Table of Contents here.